

Charge transfer and Mott-Hubbard excitations in FeBO₃: An Fe *K*-edge resonant inelastic x-ray scattering study

Jungho Kim and Yuri Shvyd'ko*

Advanced Photon Source, Argonne National Laboratory, Argonne, Illinois 60439, USA

S. G. Ovchinnikov

*Kirensky Institute, Siberian Division, Russian Academy of Sciences, 660036, Krasnoyarsk, Russia and**Reshetnev Siberian State Aerospace University, 660014, Krasnoyarsk, Russia*

(Received 27 December 2009; published 6 June 2011)

Momentum-resolved resonant inelastic x-ray scattering (RIXS) spectroscopy has been carried out successfully at the Fe *K*-edge for the first time. The RIXS spectra of a FeBO₃ single crystal reveal a wealth of information on $\simeq 1$ –10 eV electronic excitations. The IXS signal resonates when the incident photon energy approaches the pre-edge ($1s$ - $3d$) and the main-edge ($1s$ - $4p$) of the Fe *K*-edge absorption spectrum. The RIXS spectra measured at the pre-edge and the main-edge show quantitatively different dependences on the incident photon energy, momentum transfer, photon polarization, and temperature. We present a multielectron analysis of the Mott-Hubbard (MH) and charge transfer (CT) excitations, and calculate their energies. Electronic excitations observed in the pre-edge and main-edge RIXS spectra are interpreted as MH and CT excitations, respectively. We propose the electronic structure around the chemical potential in FeBO₃ based on the experimental data.

DOI: [10.1103/PhysRevB.83.235109](https://doi.org/10.1103/PhysRevB.83.235109)

PACS number(s): 78.70.En, 71.20.Be, 78.20.-e, 75.50.Ee

I. INTRODUCTION

Iron borate (FeBO₃) is a classical material with strong electron correlations having interesting magnetic, optical, and magneto-optical properties. A review of the early studies on crystal growth, structure, physical properties (magnetic, elastic, magnetoelastic, optical, and magneto-optical), and applications of FeBO₃ can be found in Ref. 1. It is among only a few known materials magnetically ordered at room temperature and transparent in the visible spectrum,^{2,3} making FeBO₃ attractive in applications for broadband visible magneto-optical devices. A number of electronic and magnetic phase transitions induced by high pressure have been observed recently: collapse of the magnetic moment of Fe³⁺ ions,^{4,5} insulator-semiconductor transition,^{6,7} and increase of the Néel temperature.⁸

Despite a great number of experimental and theoretical studies that have been performed, the electronic structure of FeBO₃ is still not completely understood. Ovchinnikov and Zabluda⁹ developed an empirical multielectron model that took all *d* orbitals into account and strong electron correlations involving *d* electrons of Fe atoms. They derived the main parameters of the band structure, such as the charge transfer (CT) gap Δ_G , Mott-Hubbard (MH) gap U_G , crystal-field splitting $10Dq$, etc., by analyzing optical absorption spectra and x-ray photoemission spectroscopy.^{7,9} The same model has been applied to interpret the high-pressure-induced magnetic collapse and insulator-metal transition.¹⁰ The first-principles local-density approximation (LDA) energy band calculations predicted an antiferromagnetic (AFM) metal instead of an AFM insulator.¹¹ Shang *et al.*¹² have performed first-principles band-structure calculations using the density functional theory within the generalized gradient approximation (GGA) and the GGA+*U* approach. The electronic structure was predicted to be high spin, antiferromagnetic, and insulating, in agreement with experiments. However, in

order to predict the correct value of the band gap in the first-principles calculation, the Coulomb repulsion $U = 7$ eV has to be assumed, much higher than $U = 2.97$ eV obtained in the empirical multielectron model of Ref. 9.

An insulating ground state in a transition metal (TM) compound is realized by a strong Coulomb repulsion between *3d* electrons. A Mott-Hubbard gap U_G is formed between a singly occupied *d* band (lower Hubbard band, LHB) and a doubly occupied *d* band (upper Hubbard band, UHB). On the other hand, when the occupied *p* band of the ligand atom moves closer to the Fermi level, the insulating charge gap is formed between the highest occupied *p* band and UHB. In the Zaanen-Sawatzky-Allen (ZSA) scheme,¹³ the TM compound is classified as a MH type in the first case and a CT type in the second case. The general trend is that early TM compounds belong to the MH type and late TM compounds, such as cuprates, belong to the CT type. For Fe compounds with half-filled *3d* level, such as FeBO₃, however, the classification is not as clear; U_G from the lowest MH excitation is comparable with Δ_G from the lowest CT excitation.

Probing CT and MH excitations is important to resolve the existing ambiguities in determination of the electronic structure and parameters in FeBO₃. Conventional spectroscopy, such as optical spectroscopy, is limited; it has difficulty in probing dipole-forbidden charge excitation, such as MH excitation, and characterization of excited charge excitation is not straightforward because it can not probe CT and MH excitations selectively. A spectroscopy that uses the excited electronic state of interest as an intermediate state can provide a way to overcome such a limitation.

Momentum-resolved resonant inelastic x-ray scattering (RIXS) at the *K*-edge plays an increasingly important role as a photon-in photon-out spectroscopic tool for investigation of localized and propagating charge excitations in TM compounds providing bulk-sensitive, element-specific information. A variety of systems, including cuprates,^{14–20}

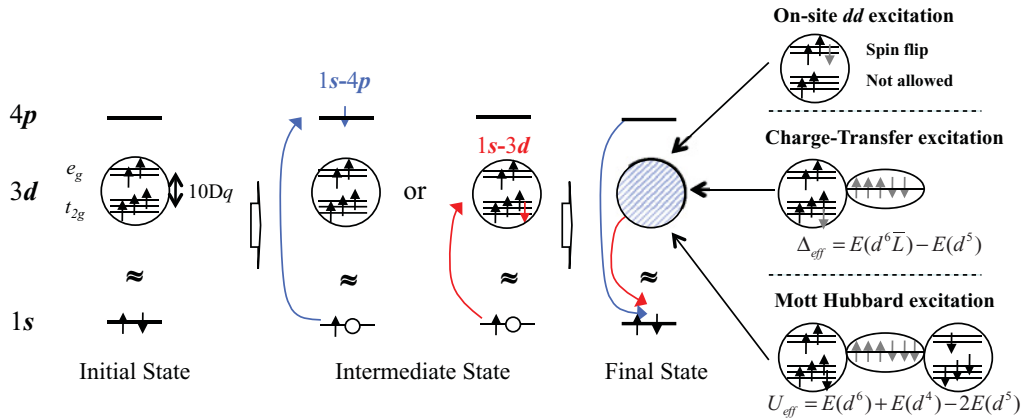


FIG. 1. (Color online) Schematic of an Fe K -edge RIXS process in FeBO₃. In the initial state, five 3d electrons fill t_{2g} and e_g crystal-field levels in the high-spin configuration. Two absorption transitions can be used for RIXS measurement: the pre-edge $1s-3d$ and the main-edge $1s-4p$. Various valence electronic excitations are left behind after the decay of the excited electron back into the $1s$ core level: on-site dd , charge transfer, and Mott-Hubbard excitations. On-site dd excitations are forbidden because of spin-selection rule.

manganites,^{21,22} and nickelates,^{23,24} have been studied by RIXS.

Figure 1 shows a schematic diagram of the Fe K -edge RIXS process in FeBO₃. In the initial state, five 3d electrons (d^5) fill t_{2g} and e_g crystal-field levels in the high-spin configuration. The empty $4p$ state is located at several electron volts above the Fermi level. By tuning the incident photon energy near the Fe K -absorption edge, the $1s$ core electron can be promoted to an empty $4p$ or $3d$ state. The intermediate state with a core hole present is unstable. The excited system quickly decays; the empty $1s$ core level is filled by an electron and a photon is emitted. The energy and momentum of the emitted photon (E_f and \vec{Q}_f) can change from those of the incident photon (E_i and \vec{Q}_i) and various valence electronic excitations, such as on-site dd , CT, and MH excitations can be left behind. Measuring RIXS spectra $S(\varepsilon, \vec{Q}, E_i)$ for a given momentum transfer $\vec{Q} = \vec{Q}_f - \vec{Q}_i$ and energy transfer $\varepsilon = E_i - E_f$ provides valuable information on valence electronic excitations in solids. The availability of two absorption transitions at the Fe K -edge provides an opportunity to probe different valence electronic excitations selectively. We will refer to the main-edge RIXS if the incident photon energy is tuned to the energy of the $1s-4p$ ($E_i \approx 7131$ eV) transition, where the underline denotes a hole. Similarly, we will refer to the pre-edge RIXS when the incident photon energy is tuned to the energy of the $1s-3d$ ($E_i \approx 7113.5$ eV) transition. CT excitations could be excited in the main-edge RIXS as a result of shakeup process due to the interaction between the core-hole and valence electrons. On the other hand, one can expect that the on-site dd and MH excitations are observed in the pre-edge RIXS because angular momentum is transferred to the $3d$ valence system via the polarization of the photon.^{25–27} However, until now, this has not been well studied experimentally.

In this paper, we explore this possibility by measuring RIXS spectra using both absorption transitions. Preliminary results were published previously.²⁸ This paper is organized as follows: Section II outlines the experimental technique and sample. The data and data analysis are presented in Sec. III, beginning with x-ray absorption spectroscopy (XAS) measurements in Sec. III A. Section III B presents E_i dependence

of RIXS including self-absorption corrections. Sections III C, III D, and III E present momentum transfer, photon polarization, and temperature-dependence measurement results, respectively. In Sec. III F, we derive E_i -independent RIXS response function from the main-edge RIXS and compare it with dielectric loss function. Multielectron analysis of the MH and CT excitations and the electronic structure around the chemical potential are presented in Sec. IV.

II. EXPERIMENTAL TECHNIQUE AND SAMPLE

The RIXS measurements were performed using the MERIX spectrometer at the XOR-IXS 30-ID beamline of the Advanced Photon Source (APS). The sample is mounted in the Displex closed-cycle cryostat DE-202N with a temperature range from 6 to 450 K. The measurements were carried out from room temperature to 355 K across the Neél temperature ($T_N = 348$ K) in FeBO₃. X rays impinging upon the sample were monochromatized to a bandwidth of 75 meV, using a four-bounce (+ - - +) monochromator with asymmetrically cut Si(400) crystals.²⁹ The beam size on the crystal was reduced to 45(H) × 20(V) μm^2 by focusing with x-ray mirrors in the Kirkpatrick-Baez configuration. The photon flux on the sample was 1.1×10^{12} ph/s. The total energy resolution of the MERIX spectrometer at the Fe K -edge is 180 meV. This is achieved by using a Ge(620) spherical diced analyzer and a position-sensitive microstrip detector placed on a Rowland circle with a 1-m radius. The silicon microstrip detector with 125 μm pitch is applied for the purpose of reducing the geometrical broadening of the spectral resolution function.³⁰ Maximum RIXS count rates were in a range of 40–50 Hz.

Figure 2 shows the measurement geometry. The angle between sample surface and incident photon propagation direction (the incidence angle) is indicated by α . Horizontal scattering geometry, where the incident photon polarization component (\vec{e}_i) is parallel to the scattering plane (π polarization), was used in all RIXS measurements. The scattered photon polarization (\vec{e}_f) is not analyzed. The FeBO₃ sample is mounted in such a way that the momentum transfer $\vec{Q} = \vec{Q}_f - \vec{Q}_i$ is parallel to the crystal c axis. The angle α , in

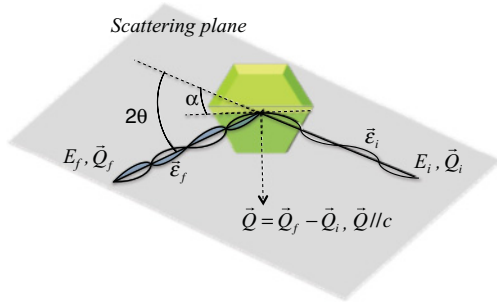


FIG. 2. (Color online) Schematic of the scattering geometry in the RIXS experiment. The FeBO_3 sample is mounted in such a way that the momentum transfer $\vec{Q} = \vec{Q}_f - \vec{Q}_i$ is parallel to the crystal c axis.

this particular case, is one half of the scattering angle 2θ . X-ray absorption spectroscopy (XAS) spectra of FeBO_3 were measured in the total fluorescence yield with a PIN diode.

FeBO_3 single crystal with low-dislocation density, grown by spontaneous crystallization from flux,³¹ was used in the current experiment. The crystal has the form of a platelet $6 \times 7 \times 0.15 \text{ mm}^3$, with the c axis perpendicular to the platelet surface. Iron borate has a rhombohedral calcite structure that belongs to the space group $R\bar{3}c(D_{3d}^6)$ with two formula units per unit cell. The lattice constants are $a = b = 4.626(1) \text{ \AA}$ and $c = 14.493(6) \text{ \AA}$. The Fe^{3+} ions are centered in a slightly distorted O_6^{2+} octahedron. The octahedral O_h crystal field splits the energy of the $3d$ orbitals into three-fold degenerate t_{2g} and two-fold degenerate e_g states. The crystal-field splitting $10Dq$ is equal to the energy separation between t_{2g} and e_g . As depicted in Fig. 1, five $3d$ electrons in the ground state fill these crystal-field levels in the high-spin configuration.⁵ The FeBO_3 is a large-gap antiferromagnetic insulator with a Néel temperature $T_N = 348 \text{ K}$ below which the two sublattice magnetic moments along the c axis order antiferromagnetically. All of the Fe^{3+} spins are in the plane perpendicular to the c axis. Nearest-neighbor (NN) exchange interaction of the Fe^{3+} spins is antiferromagnetic. A slight canting of two sublattice magnetic moments gives rise to a weak ferromagnetic moment.²

III. DATA AND ANALYSIS

A. X-ray absorption spectroscopy

Figures 3(a) and 3(b) show Fe K -edge x-ray absorption spectra in FeBO_3 measured at selected incidence angles $\alpha = 11^\circ, 22^\circ, 34^\circ$, and 46° . Two broad absorption peaks are observed in the main-edge ($1s-4p$) absorption at $E_i = 7130$ and 7137 eV . Their intensity and position have a weak dependence on α .

Figure 3(b) shows x-ray absorption spectra in the region of the pre-edge peak. Two peaks are observed, which can be assigned to $1s-3d(t_{2g})$ and $1s-3d(e_g)$ transitions in the order of increasing energy.³² A 1.4 eV energy spacing between the peaks is due to the crystal-field splitting $10Dq$ in the excited $3d$ state.³² Note that the crystal-field splitting $10Dq$ in the ground state obtained by the optical absorbance spectrum is 1.57 eV .⁹ In contrast to the main-edge absorption, the pre-edge x-ray absorption reveals significant incident angle

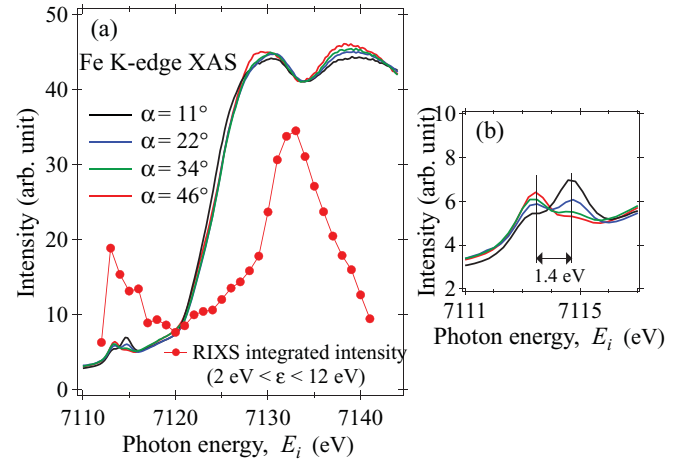


FIG. 3. (Color online) (a) Fe K -edge x-ray absorption spectroscopy (XAS) data measured at different angles of incidence α to the crystal surface (solid lines) and integrated intensities of the Fig. 4(a) RIXS spectra (red filled dots). (b) XAS data in the region of the pre-edge peak.

α dependence. The intensity of the peak corresponding to the $1s-3d(t_{2g})$ transition increases with α and is largest for angle $\alpha = 46^\circ$. The intensity of the peak corresponding to the $1s-3d(e_g)$ has an opposite dependence: it is largest at smallest incidence angle α . While the main-edge absorption is dipole allowed, the pre-edge absorption may be due to both electric quadrupole and vibronic (dynamic) or ligand-field-induced (static) electric dipole transitions. However, distinguishing dipole and quadrupole contributions from each other is not trivial, and a detailed angular study including azimuthal dependence is required to elucidate the origin of the pre-edge in FeBO_3 .³³⁻³⁵ The XAS spectra were used to correct RIXS spectra for self-absorption (SA) of the scattered photon.³⁶⁻⁴⁰

B. RIXS incident photon energy (E_i) dependence

Figure 4(a) shows RIXS spectra measured at $\vec{Q} = (0\ 0\ 9)$ with E_i changing from the pre-edge to the main-edge absorption energies. The RIXS spectra are shifted vertically for clarity. The zero intensity level for each spectrum is shown by a solid line. A strong elastic signal is observed at $\varepsilon = 0$ for all spectra. The RIXS signal resonates around $E_i = 7131$ and 7113.5 eV . Intensities of the RIXS spectra integrated in the range $2 \text{ eV} \leq \varepsilon \leq 12 \text{ eV}$ are plotted in Fig. 3(a), with two resonances clearly seen around $E_i = 7131$ and 7113.5 eV . The feature around $\varepsilon = 12 \text{ eV}$ observed for $7120 \text{ eV} < E_i < 7125 \text{ eV}$ is due to $K\beta_{2,5}$ emission corresponding to transitions from $4p$ or $3d$ to $1s$ core.⁴¹ As E_i decreases, the $K\beta_{2,5}$ emission shifts towards a lower energy with its intensity decreasing.

Figure 4(b) shows a 2D color plot of RIXS intensities in the (E_i, ε) space. For $E_i = 7131 \text{ eV}$, a strong inelastic signal is observed in the region from $\varepsilon = 4$ to 10 eV . As E_i increases, the inelastic signal on the lower energy part of the region decreases. For $E_i > 7137 \text{ eV}$, a strong inelastic signal is observed only in the narrow range around $\varepsilon \approx 10 \text{ eV}$. Similar behavior was observed earlier in a number of main-edge RIXS studies on cuprates.^{14,26,42,43} In the case of the pre-edge RIXS, the strongest inelastic signal is observed around $\varepsilon = 6 \text{ eV}$.

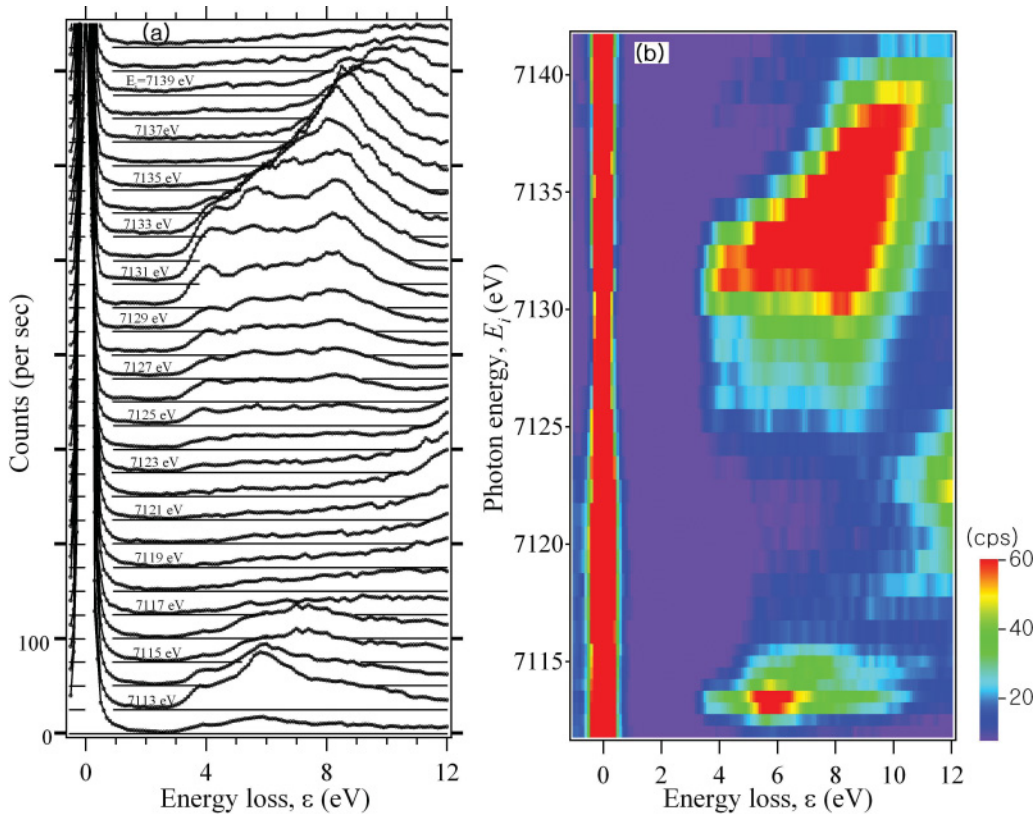


FIG. 4. (Color online) (a) RIXS spectra (vertically shifted for clarity) measured for different incident photon energies $7112 \text{ eV} \leq E_i \leq 7140 \text{ eV}$ with $\vec{Q} = (0 \ 0 \ 9)$ are plotted as a function of energy loss $\epsilon = E_i - E_f$. Self-absorption corrections for the scattered photon have been made (see the text). (b) 2D plot of the RIXS spectra shown in (a).

Figure 5(a) shows representative raw and self-absorption corrected spectra measured at the main-edge ($E_i = 7131.0 \text{ eV}$). By the correction, the first two peaks are enhanced but the third peak is diminished. Figure 5(b) shows representative raw and self-absorption corrected spectra measured at the pre-edge ($E_i = 7113.5 \text{ eV}$). No noticeable correction is observed due to the fact that absorption at the pre-edge is small.

Each corrected RIXS spectrum reveals three broad peaks as shown in Figs. 5(c) and 5(d): (M1, M2, M3) for the main-edge RIXS and (P1, P2, P3) for the pre-edge RIXS. Gaussian functions are used to fit those observed peaks, while the Voigt function is used to fit the elastic peak. In the case of the main-edge RIXS spectrum, an additional broad Gaussian function is added to fit a gradually rising background due to $K\beta_{2,5}$ emission. The peak energies and full widths at half maximum (FWHM) are shown in Table I. Peak energies from the raw RIXS spectrum are shown in parentheses. The self-absorption correction was found to have a small effect on the peak energy value.

C. RIXS momentum-transfer dependence

Figures 6(a) and 6(b) show the main-edge RIXS spectra measured at $E_i = 7131 \text{ eV}$ for different momentum transfer along the c axis, $\vec{Q} = (0 \ 0 \ L)$. For all \vec{Q} , the three peaks (M1, M2, and M3) are observed. Their peak position energies,

widths, and intensities were evaluated using the procedure described in the previous section. Gradually rising background due to the $K\beta_{2,5}$ emission is fit to a broad Gaussian peak (FWHM = 9.3 eV and $\epsilon = 13 \text{ eV}$). In the case of M3, the peak width is fixed to 2.97 eV.

The M1 and M2 peak energies are shown as a function of \vec{Q} in Fig. 7(a). Both peaks show strong oscillating \vec{Q} dependence with maxima at $\vec{Q} = (0 \ 0 \ 3)$ and $(0 \ 0 \ 9)$ and minima at $\vec{Q} = (0 \ 0 \ 6)$ and $(0 \ 0 \ 12)$. Note that $\vec{Q} = (0 \ 0 \ 6)$ corresponds to the first allowed Bragg reflection along this highly symmetric direction, and $(0 \ 0 \ 12)$ is the second one, e.g., the Brillouin zone center. Therefore, these two low-lying excitations have the normal dispersion relation showing direct energy gaps. The widths of the M1 and M2 peaks are shown as a function of \vec{Q} in Fig. 7(b). Peak widths (FWHM) are slightly smaller around $\vec{Q} = (0 \ 0 \ 6)$ and $(0 \ 0 \ 12)$.

Figures 6(c) and 6(d) show the pre-edge RIXS spectra measured $E_i = 7113.5 \text{ eV}$ for different $\vec{Q} = (0 \ 0 \ L)$. The three peaks (P1, P2, and P3) in the RIXS spectra of Fig. 6(a) were fit by three Gaussian peaks as described in the previous section. The positions of P1 and P2 are shown in Fig. 7(c). Peak energies do not show noticeable changes. The mean energy is $3.96 \pm 0.05 \text{ eV}$ and $5.85 \pm 0.03 \text{ eV}$ for P1 and P2, respectively. The widths of P1 and P2 peaks are shown as a function of \vec{Q} in Fig. 7(d). The peak widths (FWHM) do not show any significant variation either in P1 or P2.

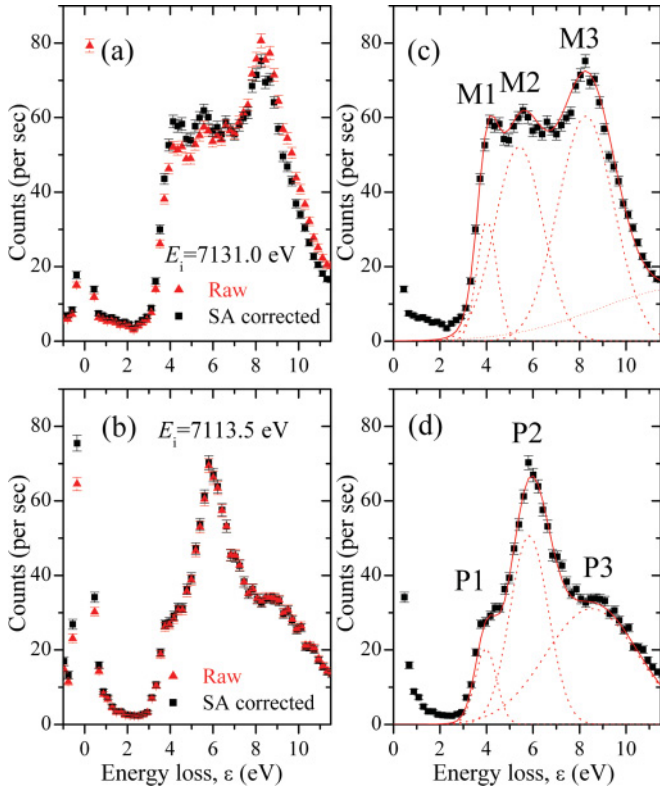


FIG. 5. (Color online) Representative RIXS spectra measured at the (a) main-edge ($E_i = 7131.0$ eV) and (b) pre-edge ($E_i = 7113.5$ eV). Raw and self-absorption corrected spectra are shown in red and black, respectively. Gaussian functions are used to fit inelastic peaks. Fit curves for the main-edge (M1, M2, M3) and pre-edge (P1, P2, P3) RIXS spectra are shown in (c) and (d), respectively.

TABLE I. Peak energies and FWHM in the self-absorption corrected RIXS spectra measured at $\vec{Q} = (0\ 0\ 9)$. Peak energies from the raw RIXS spectrum are shown in parentheses.

Main-edge RIXS	M1	M2	M3
Energy (eV)	4.10 (4.13)	5.49 (5.54)	8.32 (8.36)
FWHM (eV)	0.93	2.05	2.97
Pre-edge RIXS	P1	P2	P3
Energy (eV)	3.97	5.83	8.51
FWHM (eV)	1.07	1.93	4.65

D. RIXS photon polarization dependence

Figure 8(a) shows the elastic peak intensity change derived from fits to the main-edge and pre-edge RIXS spectra. The elastic peak intensity shows a rapid drop above $2\theta = 21.5^\circ$. This is because the polarization dependence of the elastic (Thomson) scattering cross section is proportional to the scalar product $\vec{\epsilon}_i \cdot \vec{\epsilon}_s$ of the incident and scattered photon polarization components. The large elastic peak intensity at $\vec{Q} = (0\ 0\ 6)$ is due to the tail of the first Bragg reflection.

The main-edge and the pre-edge RIXS spectra inelastic peaks show quite different intensity changes with scattering angle 2θ . Figure 8(b) shows intensity changes of the main-edge RIXS inelastic peaks. In the case of M3, the intensity starts to decrease above $2\theta = 21.5^\circ$ and shows a rapid drop above $2\theta = 43.5^\circ$. Intensities of the M1 and M2 peaks start to decrease rapidly for $2\theta > 43.5^\circ$. All inelastic intensities (M1, M2, and M3) become quite small for higher 2θ . Figure 8(c) shows the peak intensity changes of the pre-edge RIXS features. In contrast to the main-edge case, intensities of the pre-edge peaks (P1, P2, and P3) do not show any noticeable changes with 2θ .

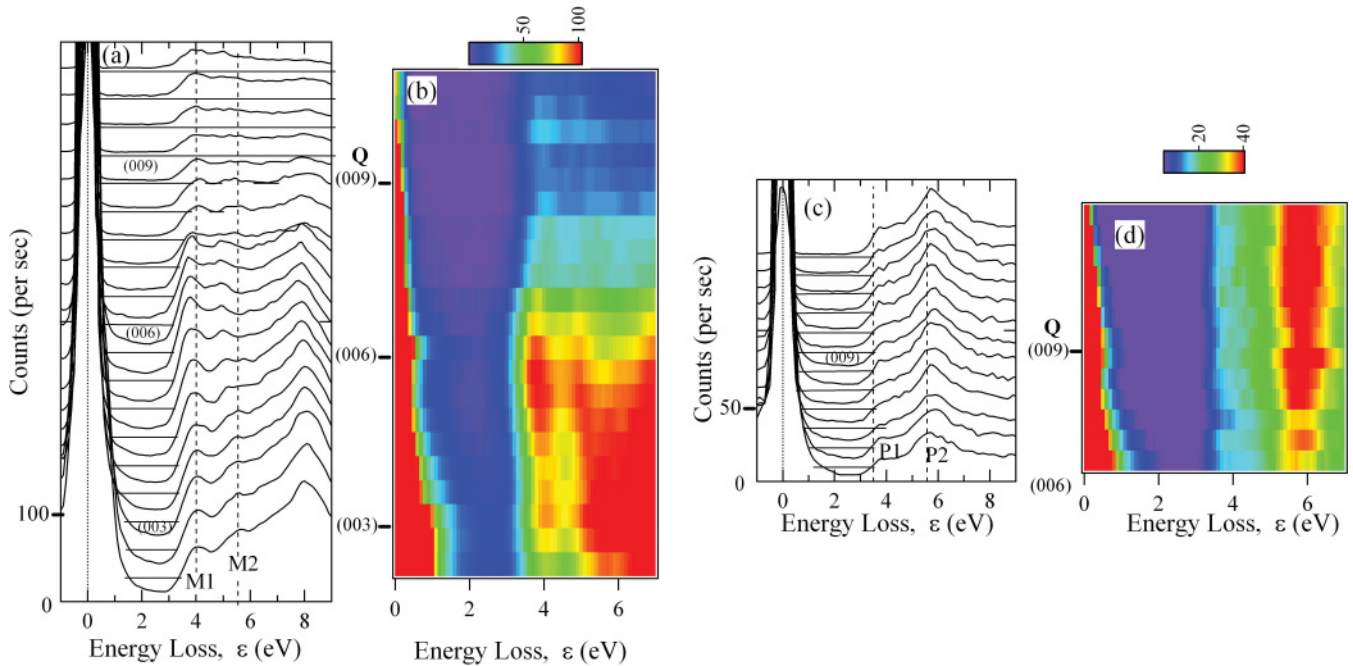


FIG. 6. (Color online) RIXS spectra measured at the (a) main-edge ($E_i = 7131$ eV), and (c) pre-edge ($E_i = 7113.5$ eV) as a function of $\vec{Q}_f = (0\ 0\ L)$, $2 < L < 11.5$. 2D plots of the corresponding RIXS data are shown in (b) and (d), respectively.

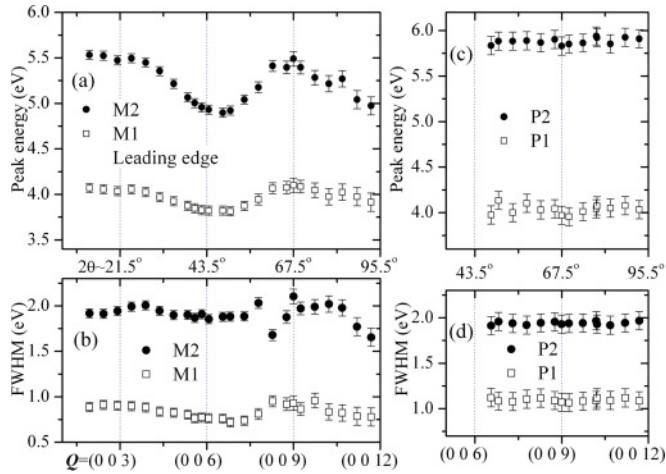


FIG. 7. (a) and (b) show peak energies and widths, respectively, of M1 and M2 as a function of \vec{Q} . Peak energies and widths of the P1 and P2 are shown in (c) and (d), respectively.

E. RIXS temperature dependence

The temperature dependence of the main-edge and pre-edge RIXS spectra were measured in the vicinity of the Néel point $T_N = 348$ K. The measurements were performed at the momentum transfer $\vec{Q} = (0\ 0\ 9)$.

Figure 9(a) shows the main-edge RIXS spectra in the energy range $2\text{ eV} \leq \varepsilon \leq 10\text{ eV}$. Figure 9(b) shows the same spectra on the energy scale in the region of the M1 peak ($2\text{ eV} \leq \varepsilon \leq 5\text{ eV}$). For a better comparison, the RIXS spectra measured at $T = 300$ K (red solid line) are superimposed on the spectra measured at higher temperatures. Within statistical error, the main-edge RIXS spectra do not show temperature dependence.

Figure 10(a) shows the pre-edge RIXS spectra in the energy range $2\text{ eV} \leq \varepsilon \leq 10\text{ eV}$. Figure 10(b) shows the pre-edge RIXS spectra in the region of the P1 peak. The RIXS spectra measured at $T = 300$ K (red) are superimposed on the spectra measured at higher temperatures. Below $T = 315$ K, no temperature dependence is observed. Between $T = 330$ and 340 K, the P1 peak becomes smaller compared with the one measured at $T = 300$ K. At higher temperatures $T = 350$ and 355 K, the P1 peak becomes broader, resulting in a decreased spectral intensity. The decrease is clearly beyond the statistical error.

F. E_i -independent RIXS response function and dielectric loss function

Recently, Ament and co-workers⁴⁴ have shown that, under assumption of a local, strong or weak, and short-lived core-hole potential, the RIXS cross section $I(\varepsilon, E_i, \vec{Q})$ can be factorized into a resonant prefactor depending on the incident (E_i) and scattered photon (E_f) energies and the dynamic structure factor $S(\varepsilon, \vec{Q})$:

$$I(\varepsilon, E_i, \vec{Q}) \sim P(\varepsilon, E_i) S(\varepsilon, \vec{Q}) \delta(\varepsilon - E_f + E_i). \quad (1)$$

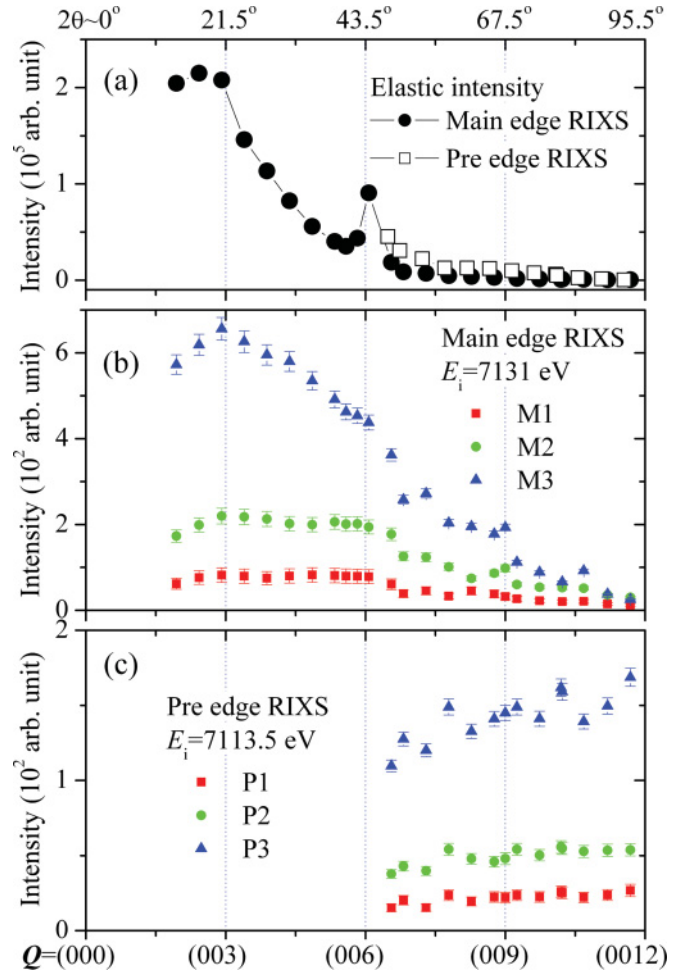


FIG. 8. (Color online) Intensity of the (a) elastic line, (b) the RIXS peaks (M1, M2, M3), and (c) (P1, P2, P3) as a function of \vec{Q} or 2θ .

The prefactor $P(\varepsilon, E_i)$ is a product of two Lorentzian functions with damping Γ_f and Γ_i due to the finite lifetime of intermediate states:

$$P(\varepsilon, E_i) = \frac{1}{[(E_f - E_{\text{res}})^2 + \Gamma_f^2/4][(E_i - E_{\text{res}} - |V|)^2 + \Gamma_i^2/4]}. \quad (2)$$

Each Lorentzian function represents resonant dependence of E_i and E_f with resonances at $E_{\text{res}} + |V|$ and E_{res} , respectively. Here, $|V|$ is the local core-hole potential. This approach to extract $S(\varepsilon, \vec{Q})$ from RIXS spectra was recently tested on a number of copper oxides (Bi_2CuO_4 , CuGeO_3 , $\text{Sr}_2\text{Cu}_3\text{O}_4\text{Cl}_2$, La_2CuO_4 , and $\text{Sr}_2\text{CuO}_2\text{Cl}_2$) by Kim and co-workers.⁴⁵ They found that the extracted $S(\varepsilon, \vec{Q})$ is in agreement with the dielectric loss-function measurement using a spectroscopic ellipsometer.

Here, we apply this approach to extract a E_i independent $S(\varepsilon, \vec{Q})$ from the main-edge RIXS spectra measured at $\vec{Q}_f = (0\ 0\ 9)$. The RIXS spectra measured at six different incident energies ($7127\text{ eV} < E_i < 7132\text{ eV}$) are used in this procedure. Parameters E_{res} , $|V|$, Γ_i , and Γ_f are determined by minimizing

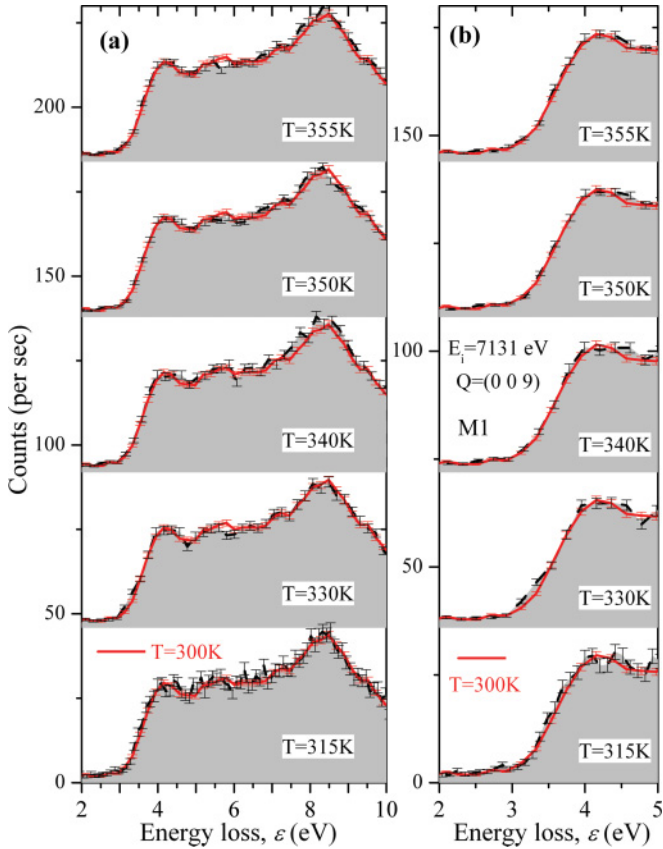


FIG. 9. (Color online) Temperature dependence of main-edge RIXS [$E_i = 7131$ eV, $\vec{Q} = (0\ 0\ 9)$] spectra (a) in the wide energy range and (b) in the region of the M1 peak.

the difference between $S[\varepsilon, \vec{Q} = (0\ 0\ 9)]$ obtained from RIXS spectra at different E_i and the averaged one. The best fit parameters are $E_{\text{res}} = 7132$ eV, $|V| = 4.4$ eV, $\Gamma_i = 3$ eV, and $\Gamma_f = 1.45$ eV.⁴⁶ Figure 11 shows $S[\varepsilon, \vec{Q} = (0\ 0\ 9)]$ calculated from Eqs. (1) and (2) with these parameters, and RIXS spectra at different E_i as dashed lines. The averaged $S[\varepsilon, \vec{Q} = (0\ 0\ 9)]$ is shown as a solid line.

Using the same fit parameters, we also derive $S[\varepsilon, \vec{Q} = (0\ 0\ 6)]$. We find that the gap energy corresponding to the onset energy of the inelastic feature is smaller in $S[\varepsilon, (006)]$ than $S[\varepsilon, (009)]$. For a comparison, the ab -plane and c -axis loss functions measured by a spectroscopic ellipsometer are plotted in Fig. 12. The ab -plane and c -axis loss functions are obtained by digitizing Fig. 1 of Ref. 47. Both loss functions show peaks around 4 eV. Increasing spectral weight at higher energy arise from higher energy peaks. The energy gap obtained from loss functions is about 3 eV. Noteworthy, we find that the gap energy of $S[\varepsilon, (006)]$ is close to that of the loss functions.

IV. DISCUSSION

Both pre-edge and main-edge RIXS spectra show no features at energies $\varepsilon < 3$ eV. This is the region where on-site dd excitation should take place. This observation is explained by spin-selection rules. In FeBO_3 five $3d$ electrons fill t_{2g} and e_g crystal-field levels in the high-spin configuration. When a single Fe^{3+} in the octahedral crystal symmetry is considered

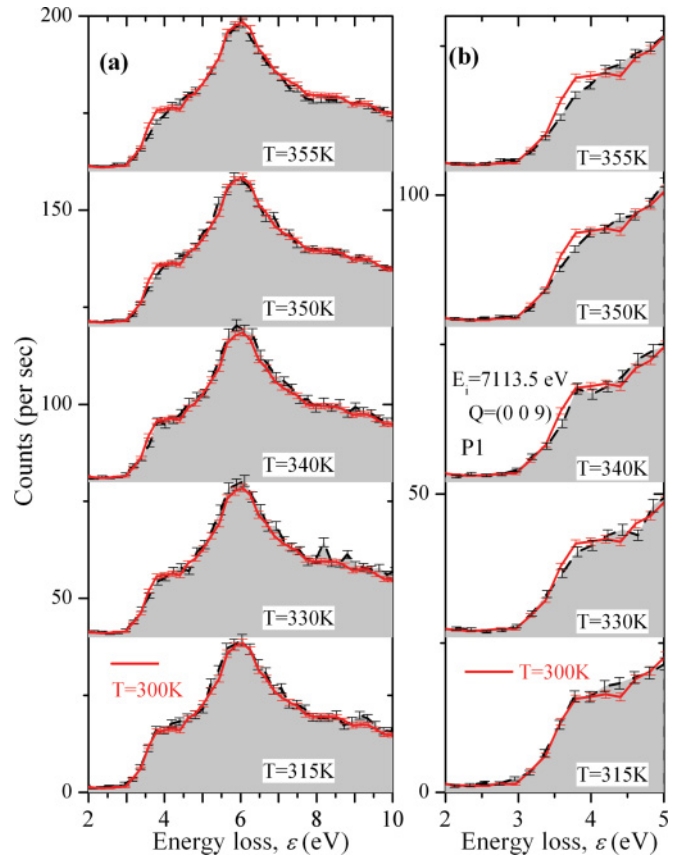


FIG. 10. (Color online) Temperature dependence of pre-edge RIXS [$E_i = 7113.5$ eV, $\vec{Q} = (0\ 0\ 9)$] spectra (a) in the wide energy range and (b) in the region of the P1 peak.

and a spin-orbit coupling in $3d$ electron is ignored, all on-site dd excitations are spin forbidden. The spin-orbit coupling of the core hole is not involved in the process of the K -edge RIXS unlike the M - and L -edge RIXS, where large spin-orbit couplings of $3p$ and $2p$ core holes give rise to mixed states of different spins. In this sense, the spin-selection rule in the

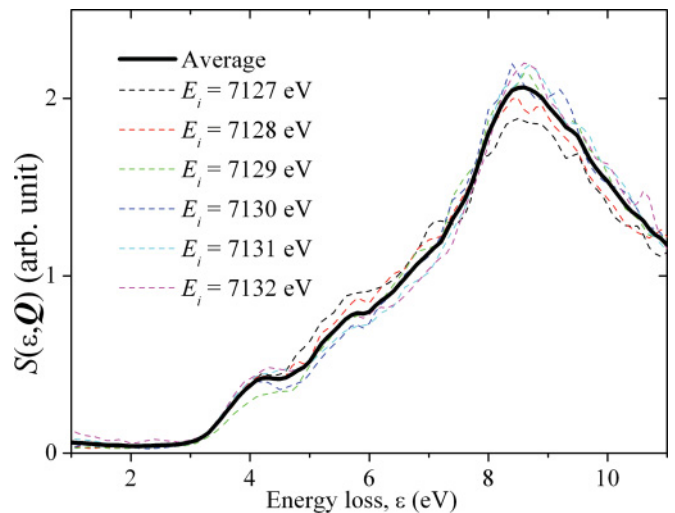


FIG. 11. (Color online) E_i -independent RIXS response function $S[\varepsilon, \vec{Q} = (0\ 0\ 9)]$ derived from main-edge RIXS spectra and Eqs. (1) and (2) (see the text).

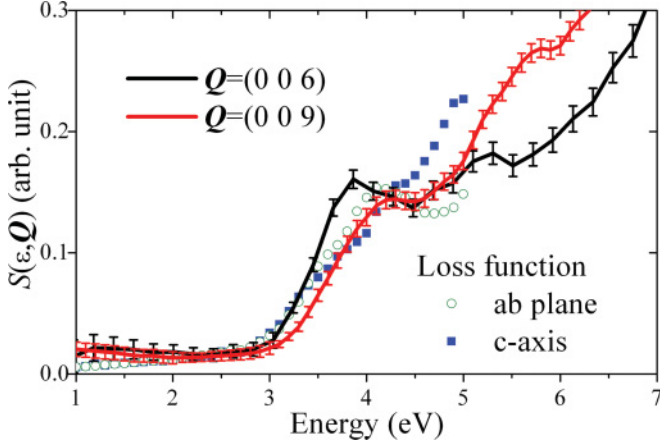


FIG. 12. (Color online) Comparison between $S(\varepsilon, \vec{Q}_f)$ extracted from measurement at $\vec{Q}_f = (0\ 0\ 6)$ and $(0\ 0\ 9)$ and the loss functions from the literature (Ref. 47).

K -edge RIXS is similar to nonresonant inelastic scattering (NIXS), where the selection rule is $\Delta S = 0$.^{48,49}

We observe that features above the optical gap ($\varepsilon > 3$ eV) are resonantly enhanced in the main-edge RIXS of FeBO_3 . This resonant enhancement has been observed in a number of main-edge RIXS studies on cuprates^{14–20,50–52} and nickelates.^{23,24} The interesting observation is that the pre-edge RIXS also leads to resonantly enhanced features at $\varepsilon > 3$ eV. Their dependence on the incident photon energy, momentum transfer, photon polarization, and temperature is different from those found in the main-edge RIXS, implying that different types of excitations are enhanced in the pre-edge RIXS.

In the following, we attempt to understand the observed RIXS features at $\varepsilon > 3$ eV and their dependence on the incident photon energy, momentum transfer, photon polarization, and temperature in terms of the MH and CT excitations. We predict excitation energies of the MH and CT of FeBO_3 in the framework of the multielectron approach.^{9,53} The influence of the FeO_6 octahedra distortion is assumed to be insignificant. $3d$ spin-orbit coupling and interatomic exchange on the excitation energy calculations are not considered. In order to obtain fine multiplet structures, an advanced step such as a multiconfiguration calculation including interactions not considered in this atomic model is necessary. Knowledge of the atomic multiplet structure is, nevertheless, helpful as a first step to understand the underlying physical process behind the observed excitations. We compared the evaluated excitation energies with the experimental data. Based on these results, the electronic structure around the chemical potential is deduced.

A. Multielectron analysis of the Mott-Hubbard and charge transfer excitations

We will use the many-electron multiband model by Ovchinnikov and Zabluda to analyze MH excitation in FeBO_3 .^{9,53} In

this model, the Hamiltonian of the system is written as

$$H = \sum_{\lambda, \sigma} \left(\varepsilon_{\lambda} n_{\lambda\sigma} + \frac{U_{\lambda}}{2} n_{\lambda\sigma} n_{\lambda\bar{\sigma}} \right) + \sum_{\substack{\lambda, \lambda' \\ (\lambda \neq \lambda')}} \sum_{\sigma, \sigma'} (V_{\lambda\lambda'} n_{\lambda\sigma} n_{\lambda'\sigma'} - J_{\lambda\lambda'} a_{\lambda\sigma}^{\dagger} a_{\lambda\sigma'} a_{\lambda'\sigma'}^{\dagger} a_{\lambda'\sigma}). \quad (3)$$

Here, λ and σ are the orbital and the spin indices, $a_{\lambda\sigma}$ ($a_{\lambda\sigma}^{\dagger}$) is the creation (annihilation) operator of d electrons with the spin σ , and $n_{\lambda\sigma} = a_{\lambda\sigma}^{\dagger} a_{\lambda\sigma}$. The quantity ε_{λ} is the atomic $3d$ level energy that may take the values of $\varepsilon(t_{2g}) = \varepsilon_d - 0.4 \times (10Dq)$ and $\varepsilon(e_g) = \varepsilon_d + 0.6 \times (10Dq)$. Coulomb intraorbital repulsion energy U_{λ} is nonzero when the $3d$ electron occupies the same orbital with the different spin. Coulomb interorbital repulsion energy $V_{\lambda\lambda'}$ is nonzero when a $3d$ electron occupies a different orbital. Hund exchange energy $J_{\lambda\lambda'}$ is nonzero when a $3d$ electron occupies a different orbital with the same spin. Neglecting the orbital dependence, these three energies are related by $U = V + 2J$. Note that this is an atomic model, ignoring $3d$ spin-orbit interaction and interatomic exchange.

The ground-state crystalline term of FeBO_3 is ${}^6A_{1g}$. Its energy $E(d^5: {}^6A_{1g})$ is equal to

$$3\varepsilon(t_{2g}) + 2\varepsilon(e_g) + 10V - 10J = 5\varepsilon_d + 10V - 10J. \quad (4)$$

The lowest d^4 configuration corresponds to occupied three t_{2g} and one e_g states in the high-spin configuration in which the crystalline term is 5E_g . Its energy $E(d^4: {}^5E_g)$ is equal to

$$3\varepsilon(t_{2g}) + \varepsilon(e_g) + 6V - 6J = 4\varepsilon_d - 6Dq + 6V - 6J. \quad (5)$$

The lowest d^6 configuration corresponds to occupied four t_{2g} and two e_g in the high-spin configuration in which the crystalline term is ${}^5T_{2g}$. Its energy $E(d^6: {}^5T_{2g})$ is equal to

$$4\varepsilon(t_{2g}) + 2\varepsilon(e_g) + U + 14V - 10J = 6\varepsilon_d - 4Dq + U + 14V - 10J. \quad (6)$$

1. Mott-Hubbard excitations

Now we can calculate the lowest MH excitation energy

$$\varepsilon_{P1} = E(d^6: {}^5T_{2g}) + E(d^4: {}^5E_g) - 2E(d^5: {}^6A_{1g}) = U + 4J - 10Dq = U_G. \quad (7)$$

Higher MH excitations are

$$\varepsilon_{P2} = E(d^6: {}^5E_g) + E(d^4: {}^5E_g) - 2E(d^5: {}^6A_{1g}) = U_G + 10Dq, \quad (8)$$

$$\varepsilon'_{P2} = E(d^6: {}^5T_{2g}) + E(d^4: {}^5T_{2g}) - 2E(d^5: {}^6A_{1g}) = U_G + 10Dq, \quad (9)$$

and

$$\varepsilon_{P3} = E(d^6: {}^5E_g) + E(d^4: {}^5T_{2g}) - 2E(d^5: {}^6A_{1g}) = U_G + 20Dq \quad (10)$$

(see Fig. 13). There are also spin-forbidden excitations such as $E(d^6: {}^1A_{1g}) + E(d^4: {}^1T_{2g}) - 2E(d^5: {}^6A_{1g})$, which are silent in the RIXS experiment.

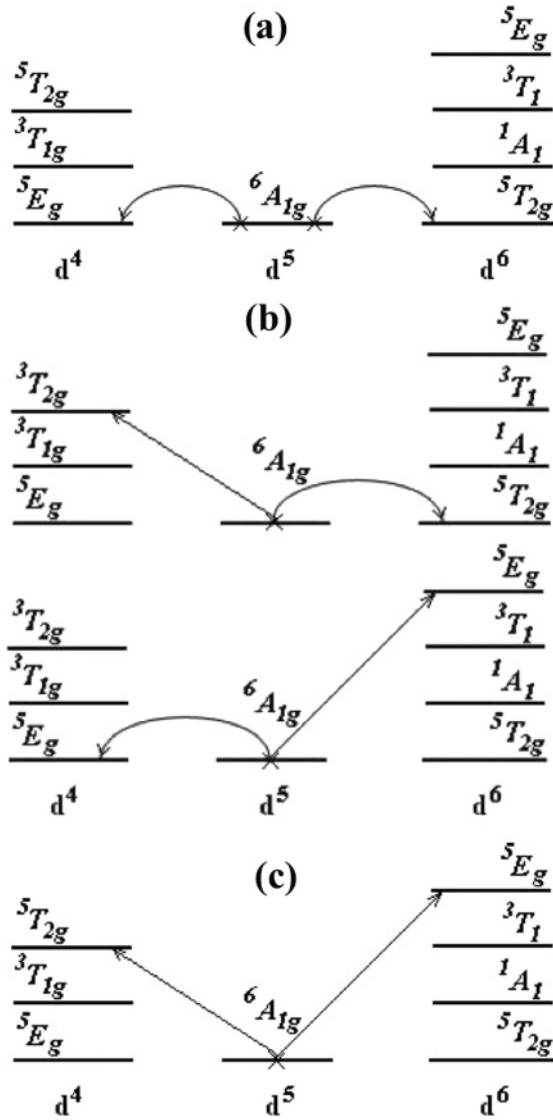


FIG. 13. Scheme of Mott-Hubbard excitations $d_i^5 d_j^5 \rightarrow d_i^4 d_j^6$, associated with (a) P1, (b) P2, and (c) P3 RIXS features. The ground-state levels $d^5(^6A_{1g})$ are marked by a cross.

All energies discussed above were calculated in the ground state. In the intermediate state of RIXS (see Fig. 1), there is the core hole with large Coulomb interaction with cation and oxygen electrons:

$$H_{1s,3d} = -V_{sd} \sum_{\lambda\sigma} n_{\lambda}^d n_{1s}, H_{1s,2p} = -V_{sp} \sum_{\mu\sigma} n_{\mu\sigma}^p n_{1s}. \quad (11)$$

Here, $n_{\lambda\sigma}^d$ ($n_{\mu\sigma}^p$) are the number of d electrons in the λ orbital (p electrons in the μ molecular orbital), and n_{1s} is the number of holes in the core orbital. In the intermediate state $n_{1s}=1$, and the interaction (10) results in the renormalization of the local energies of $3d$ and $2p$ electrons:

$$\varepsilon_d \rightarrow \varepsilon_d - V_{sd}, \quad \varepsilon_p \rightarrow \varepsilon_p - V_{sp}. \quad (12)$$

The magnitude of the Coulomb matrix elements is quite large, typically $V_{sd} \approx V_{sp} = 7$ eV. Strictly speaking, V_{sp} may be smaller due to larger screening of the $2p$ electrons. However,

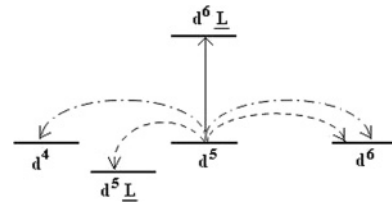


FIG. 14. Two types of the CT excitations (solid line and dotted lines), and the MH excitation (dashed-dotted lines).

in our treatment, we neglect this difference so as not to increase the number of empirical parameters. This renormalization shifts the energy of the upper Hubbard band (UHB) $\Omega_c = E(d^6 : ^5T_{2g}) - E(d^5 : ^6A_{1g})$ and the low Hubbard band (LHB) $\Omega_c = E(d^6 : ^5T_{2g}) - E(d^5 : ^6A_{1g})$. Nevertheless, the energies of the MH excitations like these shown in Fig. 13 do not depend on the core-hole Coulomb interaction.

2. Charge transfer excitations

In the multielectron approach, several channels exist for the CT excitations. The simplest one has been discussed⁵⁴: the one-electron p - d transitions from the odd-parity oxygen $\gamma_u = t_{1u}(\sigma), t_{1u}(\pi), t_{2u}(\pi)$ orbitals to the even-parity iron t_{2g} and e_g orbitals generate the many-electron transitions $d^5 \rightarrow d^6 \underline{L}$ ($d^5 : ^6A_{1g} \rightarrow d^6 : ^6T_{1u}$), which differ by crystalline term of the respective $3d^{n+1}$ configuration

$$(t_{2g}^3; e_g^2)^6 A_{1g} \rightarrow (t_{2g}^4; e_g^2)^5 T_{2g} : \underline{\gamma}_u, \quad (13)$$

$$(t_{2g}^3; e_g^2)^6 A_{1g} \rightarrow (t_{2g}^3; e_g^3)^5 E_g : \underline{\gamma}_u. \quad (14)$$

There are three strong dipole CT excitations $t_{2u}(\pi) \rightarrow t_{2g}$, $t_{1u}(\pi) \rightarrow t_{2g}$, and $t_{1u}(\sigma) \rightarrow e_g$. Thus, in the multielectron approach, we obtain the following CT excitations (Fig. 14):

$$\varepsilon_{M1} = E(d^6 \underline{L} : ^5T_{2g} t_{2u}(\pi)) - E(d^5 : ^6A_{1g}), \quad (15)$$

$$\begin{aligned} \varepsilon_{M2} &= E(d^6 \underline{L} : ^5T_{2g} t_{1u}(\pi)) - E(d^5 : ^6A_{1g}) \\ &= \varepsilon_{M1} + 1 \text{ eV}, \end{aligned} \quad (16)$$

$$\begin{aligned} \varepsilon_{M3} &= E(d^6 \underline{L} : ^5E_g t_{1u}(\sigma)) - E(d^5 : ^6A_{1g}) \\ &= \varepsilon_{M1} + 2.2 \text{ eV} + 10Dq. \end{aligned} \quad (17)$$

The numbers on the right side are just the energy differences $t_{1u}(\pi) - t_{2u}(\pi)$ and $t_{1u}(\sigma) - t_{2u}(\pi)$.^{54,55} The p - d Coulomb and exchange interactions are small (being interatomic versus intra-atomic d - d interactions), and, for the high-spin d^4 , d^5 , and d^6 configurations, they mostly compensate each other, which is why we neglect their contribution. The $d^5 \rightarrow d^6 \underline{L}$ CT excitation shown by the vertical line in Fig. 14 is similar to the standard CT excitations (see Fig. 1 of Ref. 13).

In addition, other CT excitations of the type $d^5 + d^5 \rightarrow d^5 \underline{L} + d^6$ are shown in Fig. 14 by dashed lines. Their energies are

$$\begin{aligned} \varepsilon'_{M1} &= E[d^5 \underline{L} : t_{2g}^4 e_g^1 (^4T_1) t_{2u}(\pi)] + E(d^6 : ^5T_{2g}) \\ &\quad - 2E(d^5 : ^6A_{1g}), \end{aligned} \quad (18)$$

$$\varepsilon'_{M2} = E[d^5 \underline{L} : t_{2g}^4 e_g^1 ({}^4 T_1) t_{1u}(\pi)] + E(d^6 : {}^5 T_{2g}) - 2E(d^5 : {}^6 A_{1g}), \quad (19)$$

$$\varepsilon'_{M3} = E[d^5 \underline{L} : t_{2g}^3 e_g^2 ({}^4 A_{1g}) t_{1u}(\sigma)] + E(d^6 : {}^5 T_{2g}) - 2E(d^5 : {}^6 A_{1g}). \quad (20)$$

The energies of the CT excitations [Eqs. (18)–(20)], however, are equivalent to ε_{M1} , ε_{M2} , and ε_{M3} from Eqs. (15)–(17). If we would not have neglected the small contribution $V_{pd} - J_{pd}$ of the p - d interaction, there would be a difference between the two sets of the CT excitations. We estimate this difference to be ≈ 0.1 eV, which is less than the experimental resolution.

B. Main-edge RIXS and CT excitations

In the main-edge RIXS process, a valence electron excitation is *indirectly* induced by the interaction between the core-hole and valence electrons.⁴⁴ In this process, CT excitations are expected to be enhanced because they couple strongly to intermediate states, in which charge has moved from the ligand to the TM to screen the $1s$ core hole.^{14,56} Excitations between d orbitals such as MH excitations are not expected because angular momentum can not be transferred to the $3d$ valence system. This whole process is well captured by the formalism of Ament, Forte, and van den Brink,⁴⁴ in which the RIXS response function is proportional to the dynamic structural factor or dielectric loss function. In this paper, we showed that our data can be described by this formalism, and the E_i -independent RIXS response function $S(\varepsilon, \hat{Q})$ can be obtained. In particular, the energy gap of $S[\varepsilon, \hat{Q} = (0\ 0\ 6)]$ is found to match well that of the dielectric loss functions from spectroscopic ellipsometry.

We attribute the observed peaks in the main-edge RIXS to dipole CT excitations. Two low-lying peaks, M1 and M2, disperse by 0.28 and 0.56 eV, respectively. The dispersive nature of CT excitation has been previously reported for cuprates in a number of RIXS studies.^{15,16,20,23,52,57} CT excitations in cuprates are associated with transitions from the Zhang-Rice band ($O2p$) to the upper Hubbard band (UHB). For example, the 2-eV peak of La_2CuO_4 disperses by $0.1 \sim 0.5$ eV.^{20,23,52} The observed insensitivity of the main-edge RIXS peaks to the AFM magnetic order is naturally explained because the spectral intensity of CT excitations is known to be insensitive to local magnetic correlations due to the completely filled oxygen $2p$ states.⁵⁸ Around 90° scattering angle in the horizontal scattering geometry (π polarization), the CT excitation is strongly suppressed because the incident photon polarization component is perpendicular to the scattered photon polarization component.^{27,59,60} This explains the small main-edge RIXS intensity around the 90° scattering angle.

We attribute the M1 and M2 peaks to $t_{2u}(\pi) \rightarrow t_{2g}$ and $t_{1u}(\pi) \rightarrow t_{2g}$, respectively. As shown in Table II, the observed M2 energy (4.93 eV) is in a good agreement with the theoretical value (4.82 eV). In the case of the M3 peak, we find a larger discrepancy between the experimental M3 (8.36 eV) and the theoretical value (7.59 eV). One explanation is that the M3 peak is related to a higher CT excitation, which is not considered in our theory. Another plausible origin for M3 is a

TABLE II. Peaks in the measured RIXS spectra, their assignments to the MH and CT excitations, and excitation energies from the experiment and theory. The peak energies are measured at $\hat{Q}_f = (0\ 0\ 6)$.

Peak	Assigned transition	Energy (eV)	
		Experiment	Theory
Main-edge RIXS			
M1	$t_{2u}(\pi) \rightarrow t_{2g}$	3.82	3.82
M2	$t_{1u}(\pi) \rightarrow t_{2g}$	4.93	4.82
M3	$t_{1u}(\sigma) \rightarrow e_g$	8.36	7.59
Pre-edge RIXS			
P1	$d^5 : {}^6 A_{1g} + d^5 : {}^6 A_{1g} \rightarrow d^6 : {}^5 T_{2g} + d^4 : {}^5 E_g$	3.96	3.96
P2	$d^6 : {}^5 E_g + d^4 : {}^5 E_g$	5.85	5.53
P3	$d^6 : {}^5 E_g + d^4 : {}^5 T_{2g}$	8.36	7.10

damped plasmon mode suggested in the Mn K -edge²² and Co K -edge.⁶¹ Assuming that the main-edge RIXS measures the dynamic structural factor, this damped plasmon mode could exist as nonresonant inelastic x-ray scattering.⁶² A rather broad width of the M3 peak is consistent with the damped plasmon mode.

C. Pre-edge RIXS versus MH excitations

The pre-edge RIXS enables *direct* access to the $3d$ valence system, similar to the M -edge ($3p$ - $3d$) or the L -edge ($2p$ - $3d$) RIXS (Ref. 63) but without the complexity imposed by the spin-orbit interaction. MH excitations can be observed in the pre-edge RIXS since angular momentum is transferred to the $3d$ valence system. MH excitations were theoretically predicted to be observed by RIXS (Ref. 64) and have been found in the RIXS studies on manganites, which are typical MH insulators.^{21,22,65}

We attribute the observed peaks in the pre-edge RIXS spectra to MH excitations. The pre-edge RIXS excitations show no dispersion, in contrast to the dispersive behavior of the CT excitations. The origin of the difference in dispersion is that the delocalized ligand $2p$ band has a larger bandwidth than the transition metal $3d$ band. Note that Mott-Hubbard excitations in manganites do not show any obvious dispersive behavior.^{21,22,65}

The observed temperature dependence of the pre-edge RIXS excitation can be understood by the spin-conserving MH excitation in the strong crystal-field limit. As mentioned before, five d electrons in FeBO_3 fill three-fold degenerate t_{2g} and two-fold degenerate e_g in the high-spin configuration. The Mott-Hubbard excitation in FeBO_3 is the intersite charge transfer between two neighboring Fe ion sites resulting in d^4 on one site and d^6 on the other site. In the antiferromagnetic nearest-neighbor alignment, this transition occurs easily because the NN site has the unoccupied level with the same spin with the electron at the center site. On the other hand, in the ferromagnetic NN alignment, the electron at the center site can not hop to the NN site because the unoccupied level at the NN site is in the opposite spin state. Therefore, the change in the antiferromagnetic NN alignment will be reflected in the MH excitation.

The photon polarization dependence in the TM L edge is investigated by several authors.^{59,60} They showed that the transition between the same symmetry states are forbidden in the measurement geometry of the π -polarized incident photon and $2\theta = 90^\circ$. In FeBO_3 , MH excitations involve changes in the symmetry of the electronic wave function, and so the π -polarization condition does not prevent the observation of the MH excitations at $2\theta = 90^\circ$.

We attribute P1, P2, and P3 peaks to MH excitations as shown in Fig. 13. Based on this assumption, we calculate $U_G = 3.96$ eV. We take the crystal-field parameter $10Dq = 1.57$ eV from the optical study.⁹ The typical value of the Hund coupling for Fe^{3+} , J is 0.7 eV. Then, from Eq. (7), we find the bare Hubbard $U = 2.73$ eV. By using these values, ε_{P2} and ε_{P3} energies can be calculated. As shown in Table II, the observed ε_{P2} (5.85 eV) is in agreement with the theoretical value (5.53 eV). On the other hand, we find a discrepancy between theory (7.1 eV) and experiment (8.36 eV) of ε_{P3} .

D. Electronic structure in FeBO_3

Figure 15 shows a schematic diagram of the electronic structure around the chemical potential (μ) in FeBO_3 based on the experimental data. The position of the non-bonding (NB) oxygen $O2p$ band relative to the LHB is determined by the value $\varepsilon_p - \Omega_v$, and we found the charge transfer energy $\delta = \varepsilon_p - \varepsilon_d$ from Eqs. (4), (6), and (15):

$$\delta = U + 4V - 4Dq - \varepsilon_{M1} = 1.082 \text{ eV}. \quad (21)$$

The value of the LHB energy is given by $\Omega_v = \varepsilon_d + 4(V - J) + 6Dq$. The energy separation between the LHB and $O2p$ band is equal to

$$\varepsilon_p - \Omega_v = U + 4J - 10Dq - \varepsilon_{M1} \approx 0.14 \text{ eV}. \quad (22)$$

Due to oxygen-oxygen hopping, the $O2p$ band has a dispersion. The bandwidth $2w_p$ may be estimated as $w_p = zt_{pp}$, where t_{pp} is the interatomic hopping between z nearest neighbors. For a typical value $t_{pp} = 0.2\text{--}0.4$ eV, we can estimate $w_p = 1\text{--}2$ eV. Recent density-functional-theory calculations within the generalized gradient approximation (GGA and

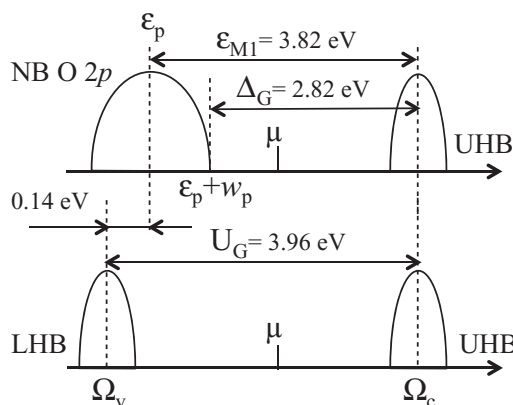


FIG. 15. Schematic of the electronic structure around the chemical potential (μ) in FeBO_3 . Energies are in the unit of eV, based on the presented RIXS measurements.

GGA+U) approach have revealed the dispersion at the top of the valence band with a width of 1 eV.¹² Thus, the value $w_p = 1$ eV will be used in our estimations. The top of the valence band has an energy of $\varepsilon_v = \varepsilon_p + w_p$. The insulating charge transfer gap $\Delta_G = \Omega_c - \varepsilon_v = \varepsilon_{M1} - w_p$. For $w_p = 1$ eV, the gap is $\Delta_G = 2.82$ eV, which is close to the gap value 2.9 eV obtained from optical absorption spectroscopy.⁶⁶ The position of the LHB inside the valence band is given by

$$\varepsilon_v - \Omega_v = U_G - \Delta_G \approx 1.14 \text{ eV}. \quad (23)$$

This parameter has been estimated as 1.4 eV by Ovchinnikov and Zabłuda.⁹ The recent, more accurate estimation based on the infrared absorption spectrum measurements in FeBO_3 results in 1.26 eV.⁶⁷ With these infrared data, the energy of the first MH excitation $U_G = 4.04$ eV, which is close to the present value $U_G = 3.96$ eV.

V. SUMMARY

In this paper, we report on the first successful resonant inelastic x-ray scattering (RIXS) studies at the K -absorption-edge of Fe. Preliminary results have been published in Ref. 28. We observe qualitatively different behaviors of the RIXS excitations associated with the main-edge and pre-edge absorption transitions. These two types of excitations have different incident energies, momentum transfers, and temperature dependences. We present a multielectron analysis of the Mott-Hubbard and charge transfer excitations, and calculate their energies. In this framework, we interpret the main-edge and pre-edge RIXS excitations as charge transfer and Mott-Hubbard excitations, respectively. This paper demonstrates effectiveness of the K -edge RIXS spectroscopy as a simultaneous probe of charge transfer and Mott-Hubbard excitations in transition metal compounds. Phenomena of the insulator-semiconductor transition and the collapse of the magnetic moment have been observed recently in FeBO_3 under pressure.⁵⁻⁷ For a detailed understanding of these phenomena, it is essential to know charge transfer energy, crystal-field splitting $10Dq$, and Coulomb repulsion U . We have demonstrated that K -edge RIXS can be used to measure these quantities directly. The K -edge RIXS, being a hard x-ray bulk-sensitive probe, can be used to study material under high pressure. It would be appealing in the next step to use these techniques to study the pressure-induced electronic and magnetic property changes in FeBO_3 .

ACKNOWLEDGMENTS

Yu.Sh. acknowledges the long-standing effort of his colleagues from the IXS Collaborative Design Team in building MERIX instrument at the XOR-IXS 30-ID beamline at the APS, in particular, J. Hill, S. Coburn (BNL), C. Burns (WMU), E. Alp, T. Toellner, and H. Sinn (APS). He is also indebted to R. Khachatryan (APS), M. Wiczyrek (APS), and A. Said (APS) for the help in manufacturing the Ge(620) analyzer. P. Siddons (BNL) is acknowledged for building the microstrip detector for the MERIX spectrometer. The help of the XOR-IXS 30-ID beamline personnel at the Advanced Photon Source:

T. Roberts, A. Said, and M. Upton are greatly appreciated. Use of the Advanced Photon Source was supported by the US DOE, Office of Science, Office of Basic Energy Sciences, under Contract No. DE-AC02-06CH11357. S.O. acknowledges the

Russian Academy of Science Physical Department program 5.7 “Strongly correlated electrons,” RFFI Grant No. 09-02-00171, RFFI Grant No. 10-02-00251, and the Siberian-Ural integration Project No. 40.

*shvydko@aps.anl.gov

- ¹R. Diehl, W. Jantz, B. J. Nöläng, and W. Wettling, *Curr. Top. Mater. Sci.* **11**, 241 (1984).
- ²A. J. Kurtzig, R. Wolfe, R. C. Lecraw, and J. W. Nielsen, *Appl. Phys. Lett.* **14**, 350 (1969).
- ³R. Wolfe, A. J. Kurtzig, and R. C. Lecraw, *J. Appl. Phys.* **41**, 1218 (1970).
- ⁴I. A. Troyan, A. G. Gavriiliuk, V. A. Sarkisyan, I. S. Lyubutin, R. Ruffer, O. Leupold, A. Barla, B. Doyle, and A. I. Chumakov, *JETP Lett.* **74**, 2001 (2001) [*Pis'ma Zh. Eksp. Teor. Fiz.* **74**, 26 (2001)].
- ⁵V. A. Sarkisyan, I. A. Troyan, M. S. Lyubutin, A. G. Gavriiliuk, and A. F. Kashuba, *JETP Lett.* **76**, 664 (2002) [*Pis'ma Zh. Eksp. Teor. Fiz.* **76**, 788 (2002)].
- ⁶I. A. Troyan, M. I. Eremets, A. G. Gavriiliuk, I. S. Lyubutin, and V. A. Sarkisyan, *JETP Lett.* **78**, 13 (2003) [*Pis'ma Zh. Eksp. Teor. Fiz.* **78**, 16 (2003)].
- ⁷A. G. Gavriiliuk, I. A. Trojan, S. G. Ovchinnikov, I. S. Lyubutin, and V. A. Sarkisyan, *JETP* **99**, 566 (2004) [*Zh. Eksp. Teor. Fiz.* **126**, 650 (2004)].
- ⁸A. G. Gavriiliuk, I. A. Trojan, I. S. Lyubutin, S. G. Ovchinnikov, and V. A. Sarkisyan, *JETP* **100**, 688 (2005) [*Zh. Eksp. Teor. Fiz.* **127**, 780 (2005)].
- ⁹S. G. Ovchinnikov and V. N. Zabluda, *JETP* **98**, 135 (2004) [*Zh. Eksp. Teor. Fiz.* **125**, 150 (2004)].
- ¹⁰I. S. Lyubutin, S. G. Ovchinnikov, A. G. Gavriiliuk, and V. V. Struzhkin, *Phys. Rev. B* **79**, 085125 (2009).
- ¹¹A. V. Postnikov, S. Bartkowski, M. Neumann, R. A. Rupp, E. Z. Kurmaev, S. N. Shamin, and V. V. Fedorenko, *Phys. Rev. B* **50**, 14849 (1994).
- ¹²S. Shang, Y. Wang, Z.-K. Liu, C.-E. Yang, and S. Yin, *Appl. Phys. Lett.* **91**, 253115 (2007).
- ¹³J. Zaanen, G. A. Sawatzky, and J. W. Allen, *Phys. Rev. Lett.* **55**, 418 (1985).
- ¹⁴P. Abbamonte, C. A. Burns, E. D. Isaacs, P. M. Platzman, L. L. Miller, S. W. Cheong, and M. V. Klein, *Phys. Rev. Lett.* **83**, 860 (1999).
- ¹⁵M. Z. Hasan, E. D. Isaacs, Z.-X. Shen, L. L. Miller, K. Tsutsui, T. Tohyama, and S. Maekawa, *Science* **288**, 1811 (2000).
- ¹⁶Y. J. Kim, J. P. Hill, C. A. Burns, S. Wakimoto, R. J. Birgeneau, D. Casa, T. Gog, and C. T. Venkataraman, *Phys. Rev. Lett.* **89**, 177003 (2002).
- ¹⁷Y.-J. Kim, J. P. Hill, H. Benthien, F. H. L. Essler, E. Jeckelmann, H. S. Choi, T. W. Noh, N. Motoyama, K. M. Kojima, S. Uchida, D. Casa, and T. Gog, *Phys. Rev. Lett.* **92**, 137402 (2004).
- ¹⁸K. Ishii, K. Tsutsui, Y. Endoh, T. Tohyama, K. Kuzushita, T. Inami, K. Ohwada, S. Maekawa, T. Masui, S. Tajima, Y. Murakami, and J. Mizuki, *Phys. Rev. Lett.* **94**, 187002 (2005).
- ¹⁹S. Suga, S. Imada, A. Higashiya, A. Shigemoto, S. Kasai, M. Sing, H. Fujiwara, A. Sekiyama, A. Yamasaki, C. Kim, T. Nomura, J. Igarashi, M. Yabashi, and T. Ishikawa, *Phys. Rev. B* **72**, 081101(R) (2005).
- ²⁰L. Lu, X. Zhao, J. N. Hancock, G. Chabot-Couture, N. Kaneko, O. P. Vajk, G. Yu, S. Grenier, Y. J. Kim, D. Casa, T. Gog, and M. Greven, *Phys. Rev. Lett.* **95**, 217003 (2005).
- ²¹T. Inami, T. Fukuda, J. Mizuki, S. Ishihara, H. Kondo, H. Nakao, T. Matsumura, K. Hirota, Y. Murakami, S. Maekawa, and Y. Endoh, *Phys. Rev. B* **67**, 045108 (2003).
- ²²S. Grenier, J. P. Hill, V. Kiryukhin, W. Ku, Y.-J. Kim, K. J. Thomas, S.-W. Cheong, Y. Tokura, Y. Tomioka, D. Casa, and T. Gog, *Phys. Rev. Lett.* **94**, 047203 (2005).
- ²³E. Collart, A. Shukla, J.-P. Rueff, P. Leininger, H. Ishii, I. Jarrige, Y. Q. Cai, S.-W. Cheong, and G. Dhalenne, *Phys. Rev. Lett.* **96**, 157004 (2006).
- ²⁴S. Wakimoto, H. Kimura, K. Ishii, K. Ikeuchi, T. Adachi, M. Fujita, K. Kakurai, Y. Koike, J. Mizuki, Y. Noda, K. Yamada, A. H. Said, and Y. Shvyd'ko, *Phys. Rev. Lett.* **102**, 157001 (2009).
- ²⁵S. Huotari, T. Pylkkanen, G. Vanko, R. Verbeni, P. Glatzel, and G. Monaco, *Phys. Rev. B* **78**, 041102(R) (2008).
- ²⁶J. Kim, D. S. Ellis, T. Gog, D. Casa, and Y.-J. Kim, *Phys. Rev. B* **81**, 073109 (2010).
- ²⁷M. van Veenendaal, X. Liu, M. H. Carpenter, and S. P. Cramer, *Phys. Rev. B* **83**, 045101 (2011).
- ²⁸Jungho Kim and Yuri Shvyd'ko, e-print arXiv:1001.1327v1.
- ²⁹T. Toellner (unpublished).
- ³⁰S. Huotari, G. Vanko, F. Albergamo, C. Ponchut, H. Graafsma, C. Henriquet, R. Verbeni, and G. Monaco, *J. Synchrotron Radiat.* **12**, 467 (2005).
- ³¹M. Kotrbova, S. Kadeckova, J. Novak, J. Bradler, G. V. Smirnov, and Y. V. Shvyd'ko, *J. Cryst. Growth* **71**, 607 (1985).
- ³²T. E. Westre, P. Kennepohl, J. G. DeWitt, B. Hedman, K. O. Hodgson, and E. I. Solomon, *J. Am. Chem. Soc.* **119**, 6297 (1997).
- ³³J. E. Hahn, R. A. Scott, K. O. Hodgson, S. Doniach, S. R. Desjardins, and E. I. Solomon, *Chem. Phys. Lett.* **88**, 595 (1982).
- ³⁴G. Dräger, R. Frahm, G. Materlik, and O. Brümmer, *Phys. Status Solidi B* **146**, 287 (1988).
- ³⁵C. Brouder, *J. Phys. Condens. Matter* **2**, 701 (1990).
- ³⁶G. Chabot-Couture, J. N. Hancock, P. K. Mang, D. M. Casa, T. Gog, and M. Greven, *Phys. Rev. B* **82**, 035113 (2010).
- ³⁷C. McGuinness, J. E. Downes, P. Sheridan, P.-A. Glans, K. E. Smith, W. Si, and P. D. Johnson, *Phys. Rev. B* **71**, 195111 (2005).
- ³⁸J. Jiménez-Mier, J. van Ek, D. L. Ederer, T. A. Callcott, J. J. Jia, J. Carlisle, L. Terminello, A. Asfaw, and R. C. Perera, *Phys. Rev. B* **59**, 2649 (1999).
- ³⁹J. Jiménez-Mier, U. Diebold, D. L. Ederer, T. A. Callcott, M. Grush, and R. C. Perera, *Phys. Rev. B* **65**, 184105 (2002).
- ⁴⁰The corrected RIXS spectra are given by multiplying the measured RIXS spectra by $1 + g \times \mu_{\text{tot}}(E_f)/\mu_{\text{tot}}(E_i)$ where $g = \sin(\alpha)/\sin(2\theta - \alpha)$, $E_f = E_i - \varepsilon$, and $\mu_{\text{tot}} = \mu_{\text{Fe}} + \mu_{\text{B, O}}$

- (Ref. 68). In our specific measurement, $g = 1$ because α is one-half of 2θ . The measured XAS is used for the total absorption cross section (μ_{tot}) where $\mu_{B,O}$ is about 10% of μ_{tot} .
- ⁴¹P. Glatzel and U. Bergmann, *Coord. Chem. Rev.* **65**, 249 (2005).
- ⁴²L. Lu, J. N. Hancock, G. Chabot-Couture, K. Ishii, O. P. Vajk, G. Yu, J. Mizuki, D. Casa, T. Gog, and M. Greven, *Phys. Rev. B* **74**, 224509 (2006).
- ⁴³Y.-J. Kim, J. P. Hill, S. Wakimoto, R. J. Birgeneau, F. C. Chou, N. Motoyama, K. M. Kojima, S. Uchida, D. Casa, and T. Gog, *Phys. Rev. B* **76**, 155116 (2007).
- ⁴⁴L. J. P. Ament, F. Forte, and J. van den Brink, *Phys. Rev. B* **75**, 115118 (2007).
- ⁴⁵J. Kim, D. S. Ellis, H. Zhang, Y.-J. Kim, J. P. Hill, F. C. Chou, T. Gog, and D. Casa, *Phys. Rev. B* **79**, 094525 (2009).
- ⁴⁶Values for V range from 2.6 to 5.7 eV and Γ from 2 to 6.4 from published works with similar approach (Refs. 14, 42, 45 and 69).
- ⁴⁷P. A. Markov, A. M. Kalashnikova, R. V. Pisarev, and T. Rasing, *JETP Lett.* **86**, 712 (2007) [*Zh. Eksp. Teor. Fiz.* **86**, 822 (2007)].
- ⁴⁸M. W. Haverkort, A. Tanaka, L. H. Tjeng, and G. A. Sawatzky, *Phys. Rev. Lett.* **99**, 257401 (2007).
- ⁴⁹N. Hiraoka, H. Okamura, H. Ishii, I. Jarrige, K. D. Tsuei, and Y. Q. Cai, *Eur. Phys. J. B* **70**, 157 (2009).
- ⁵⁰C.-C. Kao, W. A. L. Caliebe, J. B. Hastings, and J. M. Gillet, *Phys. Rev. B* **54**, 16361 (1996).
- ⁵¹J. P. Hill, C.-C. Kao, W. A. L. Caliebe, M. Matsubara, A. Kotani, J. L. Peng, and R. L. Greene, *Phys. Rev. Lett.* **80**, 4967 (1998).
- ⁵²D. S. Ellis, J. P. Hill, S. Wakimoto, R. J. Birgeneau, D. Casa, T. Gog, and Y.-J. Kim, *Phys. Rev. B* **77**, 060501(R) (2008).
- ⁵³S. G. Ovchinnikov, *JETP Lett.* **77**, 12 (2003) [*Zh. Eksp. Teor. Fiz.* **77**, 15 (2003)].
- ⁵⁴R. V. Pisarev, A. S. Moskvina, A. M. Kalashnikova, and T. Rasing, *Phys. Rev. B* **79**, 235128 (2009).
- ⁵⁵A. I. Liechtenstein, A. S. Moskvina, and V. A. Gubanov, *Sov. Phys. Solid State* **24**, 2049 (1982) [*Fiz. Tverd. Tela* **24**, 3596 (1982)].
- ⁵⁶P. M. Platzman and E. D. Isaacs, *Phys. Rev. B* **57**, 11107 (1998).
- ⁵⁷K. Ishii, K. Tsutsui, T. Tohyama, T. Inami, J. Mizuki, Y. Murakami, Y. Endoh, S. Maekawa, K. Kudo, Y. Koike, and K. Kumagai, *Phys. Rev. B* **76**, 045124 (2007).
- ⁵⁸A. Gössling, M. W. Haverkort, M. Benomar, H. Wu, D. Senff, T. Möller, M. Braden, J. A. Mydosh, and M. Grüninger, *Phys. Rev. B* **77**, 035109 (2008).
- ⁵⁹M. Matsubara, T. Uozumi, A. Kotani, Y. Harada, and S. Shin, *J. Phys. Soc. Jpn.* **69**, 1558 (2000).
- ⁶⁰M. van Veenendaal and A. J. Fedro, *Phys. Rev. Lett.* **92**, 219701 (2004).
- ⁶¹P. Leininger, J.-P. Rueff, J.-M. Mariot, A. Yaresko, O. Proux, J.-L. Hazemann, G. Vankó, T. Sasaki, and H. Ishii, *Phys. Rev. B* **74**, 075108 (2006).
- ⁶²I. G. Gurtubay, J. M. Pitarke, W. Ku, A. G. Eguiluz, B. C. Larson, J. Tischler, P. Zschack, and K. D. Finkelstein, *Phys. Rev. B* **72**, 125117 (2005).
- ⁶³W. Schülke, *Electron Dynamics by Inelastic X-Ray Scattering*, Oxford Series on Synchrotron Radiation (Oxford University Press, Oxford, 2007).
- ⁶⁴T. Idé and A. Kotani, *J. Phys. Soc. Jpn.* **69**, 1895 (2000).
- ⁶⁵K. Ishii, T. Inami, K. Ohwada, K. Kuzushita, J. Mizuki, Y. Murakami, S. Ishihara, Y. Endoh, S. Maekawa, K. Hirota, and Y. Moritomo, *Phys. Rev. B* **70**, 224437 (2004).
- ⁶⁶I. S. Edelman, A. V. Malakhovskii, T. I. Vasil'eva, and V. N. Seleznev, *Sov. Phys. Solid State* **14**, 24442 (1972) [*Fiz. Tverd. Tela* **14**, 2810 (1972)].
- ⁶⁷S. Ovchinnikov, B. Gizhevskii, N. Kazak, V. Rudenko, and A. Telegin, *JETP Lett.* **90**, 619 (2009) [*Zh. Eksp. Teor. Fiz.* **90**, 569 (2009)].
- ⁶⁸L. Tröger, D. Arvanitis, K. Baberschke, H. Michaelis, U. Grimm, and E. Zschech, *Phys. Rev. B* **46**, 3283 (1992).
- ⁶⁹G. Doring, C. Sternemann, A. Kaprolat, A. Mattila, K. Hamalainen, and W. Schulke, *Phys. Rev. B* **70**, 085115 (2004).